SCIENCE CHINA
Chemistry

•ARTICLES•

https://doi.org/10.1007/s11426-024-2574-x

Insights into host-guest interactions and enhanced MRI contrast applications of water-soluble tetrahedral metal-organic cages

Yu-Xiao Chen[1†], Mao-Song Qiu[2,3†], Jie-Sheng Hu[1], Hua-Liang Yue[1], Meng Yu[1*], Shi-Zhen Chen[2,3,4*], Xin Zhou[2,3,4] & Jun Tao[1*]

[1]*Key Laboratory of Cluster Science of Ministry of Education, School of Chemistry and Chemical Engineering, Beijing Institute of Technology, Beijing 102488, China*

[2]*State Key Laboratory of Magnetic Resonance Spectroscopy and Imaging, National Center for Magnetic Resonance in Wuhan, Wuhan Institute of Physics and Mathematics, Innovation Academy for Precision Measurement Science and Technology, Chinese Academy of Sciences, Wuhan 430071, China*

[3]*University of Chinese Academy of Sciences, Beijing 100049, China*

[4]*School of Biomedical Engineering, Hainan University, Haikou 570228, China*

Received November 14, 2024; accepted February 14, 2025; published online March 21, 2025

Metal-organic cages (MOCs) are emerging as pivotal components in the design of innovative magnetic resonance imaging (MRI) contrast agents. This study introduces a novel, water-soluble metal-organic cage, $K_{12}[Fe_4L_4]$, synthesized using a co-planar triangular ligand, *N*-{4-[4,6-bis(4-{[(2,3-dihydroxyphenyl)carbonyl]amino}phenyl)-1,3,5-triazin-2-yl]phenyl}-2,3-dihydroxybenzamide (H_6L). This cage represents the first instance of a gadolinium(III)-free M_4L_4 structure optimized for T_1-weighted imaging. We provide a detailed analysis of its structural attributes, aqueous stability, magnetic properties, and host-guest interactions. Relaxometric evaluations *in vitro* reveal that $K_{12}[Fe_4L_4]$ significantly elevates the longitudinal relaxivity of water protons, achieving a relaxivity of 5.41 mM^{-1} s^{-1} at 33 °C and 0.5 T. This enhancement increases to 9.24 mM^{-1} s^{-1} in the presence of human serum albumin (HSA), indicating potent interaction dynamics with binding constant (K_a) of $(6.1 \pm 1.4) \times 10^4$ M^{-1}. Comparative studies highlight that even at low doses of 0.010 mmol kg^{-1}, $K_{12}[Fe_4L_4]$ surpasses the imaging efficacy of the commercial agent ProHance, while also demonstrating prolonged *in vivo* retention suitable for extended diagnostic procedures. These findings not only underscore the utility of M_4L_4 cages in T_1-weighted MRI but also lay foundational insights for the development of multinuclear, gadolinium(III)-free contrast agents, paving the way for safer and more effective diagnostic imaging solutions.

tetrahedral metal-organic cages, MRI contrast agents, T_1-weighted imaging, gadolinium(III)-free agents, host-guest interactions, magnetic properties

Citation: Chen YX, Qiu MS, Hu JS, Yue HL, Yu M, Chen SZ, Zhou X, Tao J. Insights into host-guest interactions and enhanced MRI contrast applications of water-soluble tetrahedral metal-organic cages. *Sci China Chem*, 2025, 68, https://doi.org/10.1007/s11426-024-2574-x

1 Introduction

Magnetic resonance imaging (MRI) contrast agents are essential for improving diagnostic accuracy in a wide range of clinical applications [1,2]. Traditional T_1-weighted MRI contrast agents, primarily hydrophilic metal-based chelates, enhance image contrast by modulating the relaxation times of bulk water molecules (Scheme 1) [1,3]. The efficacy of these agents is significantly influenced by the paramagnetic properties of the metal ions they contain. Specifically, the effectiveness of paramagnetic-induced T_1 relaxation corre-

†Equally contributed to this work.
*Corresponding authors (email: mengyu@bit.edu.cn; chenshizhen@wipm.ac.cn; taojun@bit.edu.cn)

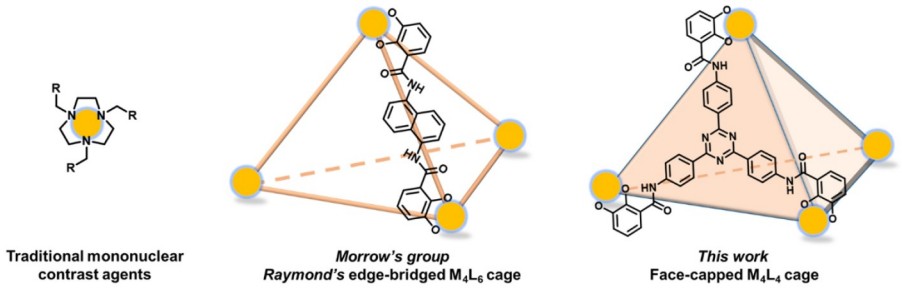

Scheme 1 (Color online) Examples of Fe(III)-based T_1-weighted contrast agents.

lates directly with the spin quantum number (S) of the metal ion, with commonly used metals including Gd(III) (S = 7/2) [4], and high-spin Fe(III) (S = 5/2) [5] and Mn(II) (S = 5/2) [6]. Among these, Gd(III)-based contrast agents (GBCAs) are the most extensively used due to their exceptional imaging capabilities. This superior performance is largely due to Gd(III)'s long electronic relaxation time (τ_e), which occurs on the scale of nanoseconds and is enhanced by its symmetric electronic ground state. This characteristic facilitates efficient nuclear T_1 relaxation, rendering GBCAs particularly effective in clinical imaging. However, the widespread adoption and generally accepted safety of GBCAs have been challenged by emerging concerns over their potential adverse effects. A seminal study in 2006 linked GBCAs to nephrogenic systemic fibrosis (NSF), a rare yet severe condition, in patients with renal dysfunction [7,8]. More recently, investigations have identified residues of Gd(III) in the brains of patients post-MRI, highlighting significant worries regarding the long-term retention of this non-endogenous element [9]. These discoveries have catalyzed a critical evaluation of GBCAs and underscored the imperative need to explore alternative contrast agents that do not rely on Gd(III), aiming to mitigate potential risks while maintaining diagnostic efficacy.

Iron, an abundant and biologically integral metal, emerges as a promising candidate for the development of Gd(III)-free MRI contrast agents. Preliminary research has concentrated on mononuclear Fe(III) macrocyclic complexes, demonstrating that high-spin Fe(III) can be stabilized under the reducing conditions of biological systems through meticulous ligand design [10,11]. However, these Fe(III)-based agents often show longer water relaxation times in solution compared to their Gd(III) counterparts, yielding suboptimal *in vivo* contrast [12]. This diminished effectiveness primarily arises from a reduced number of unpaired electrons and shorter τ_e [1]. To overcome this challenge, enhancing the number of metal ions within the contrast agent has been proposed. Notably, dinuclear Fe(III) complexes, interconnected by benzene rings, have exhibited a 2- to 3-fold improvement in proton relaxation rates [13]. While this strategy holds potential, it also introduces complexity in ligand synthesis and may adversely affect the water solubility of the complexes [14]. These factors present significant hurdles in the development of efficient multinuclear Fe(III)-based MRI contrast agents, requiring innovative solutions to balance efficacy with practical application constraints.

Metal-organic cages (MOCs) are intricate self-assembled structures formed by coordinating metal ions with organic ligands [15–21]. These cages typically incorporate multiple metal centers and are constructed using ligands that are relatively simple to synthesize [22]. The internal cavities of MOCs facilitate a rich host-guest chemistry, making them versatile platforms for a range of functional applications, including their potential as multinuclear and multifunctional MRI contrast agents [23]. Despite their promising attributes, the development of water-soluble and aqueous-stable MOCs suitable for MRI applications presents a formidable challenge. Current research in this area is still in its infancy, with only a limited number of studies reported [24,25]. In a pioneering study, Morrow's group [25], inspired by Raymond's tetrahedral Fe_4L_6 cage [26,27], introduced the first and only MOC that functions as a T_1-weighted MRI contrast agent, demonstrating excellent *in vivo* tumor imaging performance.

The structural design of MOCs, such as the choice between triangular and linear ligands, crucially impacts their stability and functionality. Edge-sealed M_4L_6 cages with linear ligands typically show reduced stability due to less effective cooperative binding mechanisms. In contrast, face-capped M_4L_4 cages, which require multiple bond disruptions for ligand dissociation, demonstrate enhanced robustness [28]. Furthermore, the open cavities of M_4L_6 cages allow the accommodation of larger guest molecules but also feature wider channels that may lead to faster guest exchange, potentially diminishing the retention of functional molecules. Dmochowski's group has utilized this property to achieve innovative designs, employing a paramagnetic organocobalt capsule with xenon host-guest chemistry to achieve hyper-CEST [29]. On the other hand, M_4L_4 cages, with their face-capped triangular panels, foster extensive non-covalent interactions between the host and guest, leading to slower

exchange rates. This characteristic is vital for stabilizing guest molecules, rendering M_4L_4 cages particularly beneficial for applications requiring sustained molecular retention, such as drug delivery.

In this study, we detail the synthesis and characterization of two novel face-capped M_4L_4 cages, where M represents Fe(III) or Ga(III). These cages are constructed using *N*-{4-[4,6-bis(4-{[(2,3-dihydroxyphenyl)carbonyl]amino}phenyl)-1,3,5-triazin-2-yl]phenyl}-2,3-dihydroxybenza-mide (H_6L) as the ligand. The ligand's tri-catechol moieties significantly enhance the structural stability and water solubility of the Fe_4L_4 cage. The core of the ligand, consisting of a central triazine unit and three attached benzene rings, forms a conjugated C_3-symmetric pseudo-coplanar structure, which acts as the face panel in these M_4L_4 cages. This configuration is pivotal for maintaining the integrity of the cage and optimizing its functionality as an MRI contrast agent. Furthermore, the internal cavity of each cage offers a versatile platform for additional functionalization, permitting modifications that tailor the cage's properties for specific imaging applications. Extensive evaluations of the solution stability, magnetic properties, host-guest chemistry, and both *in vitro* and *in vivo* imaging capabilities have been conducted. The results highlight the crucial role of structural design in optimizing these MOCs for T_1-weighted MRI applications. To our knowledge, this research represents the first instance of utilizing an M_4L_4 cage as an MRI contrast agent, paving the way for the development of multinuclear, multifunctional non-GBCAs.

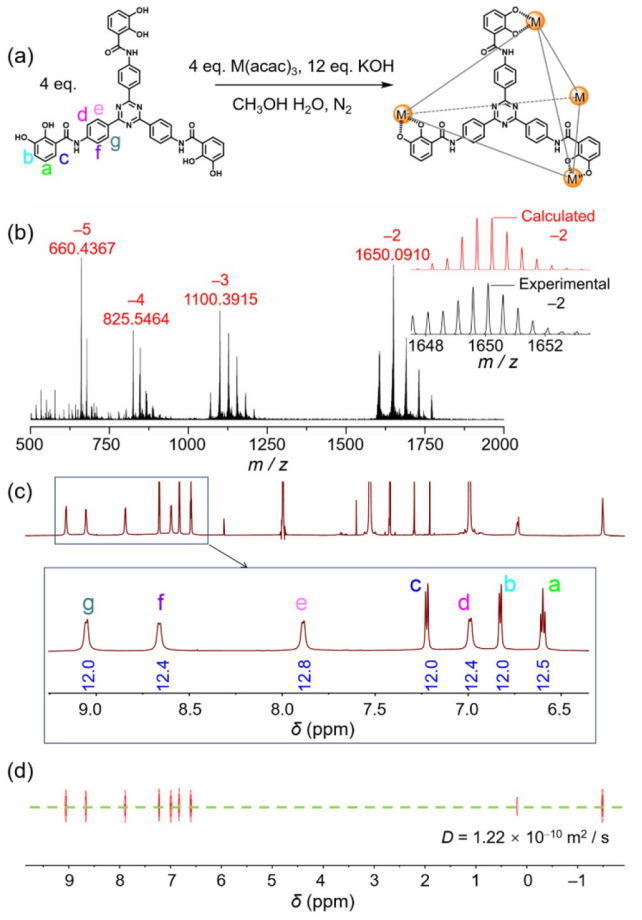

Figure 1 (Color online) (a) Self-assembling of H_6L with Ga(III) or Fe(III); (b) ESI(−)-TOF-MS of Fe_4L_4 with the inset showing the observed and simulated isotopic patterns of the −2 peak. (c) ^{1}H NMR spectrum (700 MHz, D_2O/dimethyl sulfoxide (DMSO-d_6) = 9:1, 298 K) of $(NEt_4)_{12}$-$[Ga_4L_4]$ with inset showing the details of the aromatic region; (d) DOSY spectrum of $(NEt_4)_{12}[Ga_4L_4]$.

2 Results and discussion

2.1 Syntheses and structural characterization

The synthesis of ligand started with the condensation reaction between the amino precursor and the acyl chloride precursor, yielding Me_6L (Figures S1 and S2 for NMR spectra, Supporting Information online). This intermediate was subsequently demethylated to form H_6L (Figures S3–S5 for nuclear magnetic resonance (NMR) spectra and mass spectra) by treatment with an excess of BBr_3 at −78 °C under a nitrogen atmosphere (Scheme S1, Supporting Information online). The MOCs were then synthesized by reacting 4 equiv. of H_6L with 4 equiv. of $M(acac)_3$ (where M = Fe or Ga) and 12 equiv. of KOH in a 1:1 methanol/water mixture. This reaction produced a reddish-brown or yellow mixture, depending on the metal ion used. Following centrifugation to separate insoluble impurities, the solvent was removed under reduced pressure, yielding the crude product. This crude product was subsequently redissolved in a methanol-water mixture and subjected to purification through precipitation with ether. The final product, obtained as a black or yellowish powder, is designated as $K_{12}[Fe_4L_4]$ or $K_{12}[Ga_4L_4]$, respectively, as illustrated in Figure 1a and detailed in Scheme S2. Additionally, the $(NEt_4)_{12}[Ga_4L_4]$ analogue was synthesized via a similar protocol with the addition of 12 equiv. of NEt_4Cl. The formation of this complex was confirmed by ^{1}H NMR analysis (see below).

The purity of the product was confirmed using three complementary analytical techniques: inductively coupled plasma optical emission spectroscopy (ICP-OES), which showed 96% Fe content; high-resolution mass spectrometry; and electron paramagnetic resonance (EPR) spectroscopy (Section 2.2). High-resolution electrospray ionization time-of-flight (ESI-TOF) mass spectrometry of $K_{12}[Fe_4L_4]$ in solution revealed molecular ion peaks for $\{KH_{(11-z)}[Fe_4L_4]\}^{z-}$ with charge states ranging from 2 to 5 (Figure 1b). The ^{1}H NMR spectrum of $K_{12}[Fe_4L_4]$ exhibited no discernible features, a common characteristic for high-spin Fe(III) complexes, which typically exhibit severe line broadening. This effect is attributed to rapid proton relaxation driven by paramagnetic relaxation enhancement (PRE) (Figure S6).

Given the challenges associated with the paramagnetic nature of high-spin Fe(III), Ga(III) was selected as a suitable diamagnetic analog for comparative studies due to its similar physical properties, such as an almost equivalent octahedral ion radius (0.620 Å for Ga^{3+} versus 0.645 Å for high-spin Fe^{3+}) and comparable electron affinity and ionization potentials (30.71 and 64 eV for Ga^{3+}, respectively, versus 30.65 and 54.8 eV for high-spin Fe^{3+}) [30]. Consequently, the diamagnetic congener $(NEt_4)_{12}[Ga_4L_4]$ was synthesized using NEt_4^+ as both a templating agent and counter cation. This facilitated detailed NMR spectroscopic studies aimed at elucidating the solution structural characteristics of the M_4L_4 cages.

The ^{1}H NMR spectra of $K_{12}[Ga_4L_4]$ and $(NEt_4)_{12}[Ga_4L_4]$ depicted in Figure S7 and Figure 1c, respectively. Figure 1c exhibits seven distinct resonances within the aromatic region, indicative of a highly symmetrical molecular structure. To confirm the uniformity of the species in solution, ^{1}H diffusion-ordered spectroscopy (^{1}H DOSY) spectroscopy was conducted. The DOSY results showed identical diffusion coefficients for all aromatic resonances, corroborating the formation of a single, symmetric species (Figure 1d). The hydrodynamic diameter, calculated using the Stokes-Einstein equation [31], was determined to be 36.6 Å. This measurement is consistent with its crystal structure dimensions (~23 Å) (see below). Further structural insights were obtained through ^{1}H-^{1}H COSY and ^{1}H-^{1}H nuclear Overhauser effect spectroscopy (^{1}H-^{1}H NOESY) spectroscopies (Figures S8 and S9). Notably, the proton signals from the benzene ring linked directly to the central triazine ring displayed splitting. This observation suggests a propeller-like arrangement of the three benzene rings, where aromatic protons facing outward and inward experience distinct chemical environments. The spatial interactions captured in the ^{1}H-^{1}H NOESY spectrum, particularly between protons resonating (δ) at 8.85 ppm (doublet) and 6.79 ppm (doublet), as well as 8.47 ppm (doublet) and 7.69 ppm (doublet), provide compelling evidence for the formation of the M_4L_4 cage structure.

The ^{1}H NMR spectrum reveals a distinct distribution of NEt_4^+ counterions within the upfield region (Figure 1c), where the twelve counterions split into two groups at a ratio of 11:1. The predominant group of NEt_4^+ ions exhibited peaks at δ = 2.49 ppm (quartet) and δ = 0.72 ppm (triplet), while a minor set was substantially shifted upfield, appearing at δ = 0.18 ppm (multiplet) and δ = −1.49 ppm (triplet). According to the literature, these specific resonances and their integrations are indicative of the encapsulation of NEt_4^+ counterions by the cage host [27], where the upfield shift in the NEt_4^+ resonances can be attributed to shielding effects from the aromatic ring currents of the cage facets [32]. Moreover, the $–CH_2–$ resonances of the encapsulated NEt_4^+ do not present as a simple quartet; instead, they appear as a complex multiplet, suggesting that the $–CH_2–$ groups are rendered diastereotopic within the chiral environment of the cage. This spectral feature provides strong evidence that the cage assembly is homochiral, exhibiting either all Δ or all Λ coordination at the metal vertices. This arrangement leads to a molecular symmetry consistent with the pure rotation group *T*, indicative of a racemic mixture of ΔΔΔΔ and ΛΛΛΛ cages. These findings align with the molecular symmetry observed in the single-crystal structure analysis (see below).

Despite repeated attempts, suitable single crystals of Fe_4L_4 for X-ray diffraction analysis could not be obtained. However, yellowish block crystals of $(NEt_4)_{12}[Ga_4L_4]$ were successfully grown via slow evaporation of a saturated methanolic solution, allowing for detailed structural analysis. Single-crystal X-ray diffraction (SCXRD) unambiguously confirmed the structural identity of the M_4L_4 cage, which crystallizes in the triclinic space group $R\bar{3}$. In the crystal structure, four Ga(III) centers are tetrahedrally bridged by four ligands, each forming a face of the tetrahedron with a C_3-symmetric arrangement (Figure 2). The asymmetric unit reveals that each Ga(III) center is coordinated by six oxygen atoms from the catechol groups, forming a pseudo-octahedral $[GaO_6]$ coordination geometry, which exhibits two pairs of enantiomers with individual cage exhibiting an ΛΛΛΛ or ΔΔΔΔ conformation. The structure features significant distortions from planarity among the catecholamides, despite hydrogen bonding interactions between the amide protons and the phenolic oxygens, which accommodate the trigonal prismatic coordination geometry around the Ga(III) centers. The intermetallic distances range between 17.5 and 17.8 Å, placing the overall dimension of the cage within the nanometer scale. The central cavity volume of the cage, calculated to be 264.8 $Å^3$, is smaller than the 315.9 $Å^3$ observed in the M_4L_6 cages assembled with edge-bridged ligands reported by Raymond *et al*. [25] (Figure S10). The face-capped ligand arrangement nearly completely encloses the cage's cavity, accommodating a NEt_4^+ counterion. Furthermore, the phenyl rings of each ligand are slightly tilted relative to the coplanarity with the central triazine ring, creating a propeller-like arrangement with average dihedral angles of about 4.2°. This configuration positions phenyl protons from adjacent tetrahedral panels into close proximity ($d_{H60\cdots H89}$ = 2.700 Å, $d_{H61\cdots H90}$ = 3.600 Å) (Figure S11), corroborating the nuclear Overhauser effect (NOE) interactions observed in the NMR study (Figure S9). It should be noted that Raymond's group reported a coordination cage with a similar structure, where the ligand's central aromatic ring was a benzene ring instead of a triazine ring; however, a crystal structure was not obtained in their case [33].

2.2 Magnetic properties

To further understand the magnetic characteristics of the $K_{12}[Fe_4L_4]$ cages, we commenced with an analysis of the

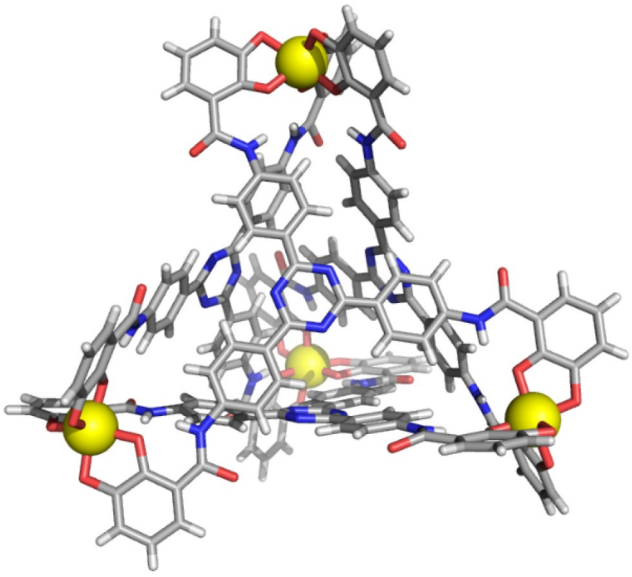

Figure 2 (Color online) Crystal structure of $(NEt)_{12}[Ga_4L_4]$ at 100 K. Cations and lattice solvent molecules were omitted for clarity. Color code: C, gray; H, white; N, blue; O, red; Ga, dark salmon.

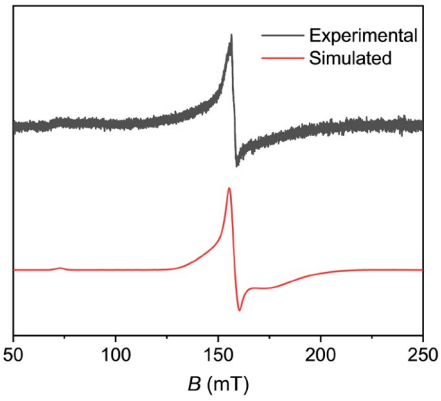

Figure 3 (Color online) EPR spectrum of $K_{12}[Fe_4L_4]$ in a 10:1 mixture of water and glycerol at 100 K. Fitting parameters: g (average) = 1.97049, Gaussian line broadening = 2.46408 mT, D = 0.06755 cm^{-1}, E = 0.01660 cm^{-1}, D-strain = 0.02665 cm^{-1}, E-strain = 0.002637 cm^{-1}.

solid-state magnetic susceptibility. At 300 K, the magnetic susceptibility ($\chi_M T$) was measured to be 15.5 cm^3 mol^{-1} K, aligning with expectations for a tetrahedral cage containing four non-interacting high-spin Fe(III) metal centers (theoretical spin-only $\chi_M T$ value for each S = 5/2 Fe(III) ion is 4.375 cm^3 mol^{-1} K) (Figure S12) [34]. Additionally, the magnetic moment of $K_{12}[Fe_4L_4]$ in solution was quantified using Evans' method, yielding a magnetic moment (μ_{eff}) of 5.4 μ_B per Fe(III) ion (Figure S13). This suggests the preservation of the high-spin state of Fe(III) in the solution environment. To probe the spin-state identity of the Fe(III) centers within $K_{12}[Fe_4L_4]$ further, EPR spectroscopy was employed. The EPR spectrum of a 1 mM solution of $K_{12}[Fe_4L_4]$ in a 10:1 mixture of water and glycerol at 100 K displayed an anisotropic asymmetric signal at $g \approx 4.25$, accompanied by a weak transition at $g \approx 9.6$ (Figure 3). These signals are indicative of the middle and upper Kramer's doublets in the low-field limit and can be modeled successfully by a S = 5/2 species with rhombic symmetry (D = 0.0676 cm^{-1}, E = 0.0166 cm^{-1}, E/D = 0.24), typical for Fe(III) catecholate complexes in a tris-coordination environment, $[Fe(cat)_3]^{3-}$ [35]. The broad features observed in the EPR spectrum necessitated the introduction of D-strain parameters, suggesting that the dynamic 'breathing' of the cage framework, induced by collision or hydrogen bonding with solvent molecules, leads to random distortions in the coordination geometry around the Fe(III) centers. This results in a distribution of D and E values. Notably, the absence of splitting features around $g \approx 4.25$ supports the lack of Fe(III) bis-catecholate impurities, which would typically arise from ligand dissociation.

2.3 Aqueous stability

The ultraviolet-visible (UV-vis) spectroscopy of $K_{12}[Fe_4L_4]$ revealed a distinct ligand-to-metal charge transfer (LMCT) band at 501 nm with a molar extinction coefficient of 13,450 M^{-1} cm^{-1}. This LMCT band is characteristic of tri-catecholate Fe(III) complexes and aligns with data reported in prior studies. To assess the stability of $K_{12}[Fe_4L_4]$ under physiological conditions, we monitored changes in the LMCT band upon exposure to excess human serum albumin (HSA), Zn^{2+}, or ethylenediaminetetraacetic acid ($EDTA^{2-}$) in 2-[4-(2-hydroxyethyl)piperazin-1-yl]ethane-1-sulfonic acid (HEPES) or phosphate buffer saline (PBS) buffer solutions at pH 7.4 and 37 °C over periods of 12 and 24 h. The results, depicted in Figures S14–S17, demonstrate no significant alterations in the UV-vis spectra, underscoring the exceptional aqueous stability of $K_{12}[Fe_4L_4]$. In addition, the $K_{12}[Fe_4L_4]$ complex exhibited acid/base stability in aqueous solution, maintaining its structural integrity under both basic and mildly acidic conditions (Figure S18). This stability is crucial for potential *in vivo* imaging applications. Further insights into the stability of MOCs were drawn from work by Nitschke and colleagues, who established a positive correlation between ligand topicity and the aqueous stability of these structures [36]. The tritopic ligand system employed in $K_{12}[Fe_4L_4]$, in comparison to the ditopic ligand system developed by Raymond, is hypothesized to confer enhanced stability. This enhancement is attributed to the increased binding cooperativity of the tritopic ligand, where dissociation necessitates the disruption of a greater number of coordination bonds.

Redox stability is pivotal for Fe(III)-based MRI contrast agents due to their propensity to participate in redox reactions with biologically relevant reductants such as ascorbic acid and glutathione [37]. These reactions can reduce high-spin Fe(III) to Fe(II), resulting in a marked decrease in MRI

contrast efficacy due to the shorter electronic relaxation time of Fe(II). Additionally, this reduction process can initiate harmful Fenton chemistry, which poses further challenges for clinical use [38]. To investigate the redox behavior of $K_{12}[Fe_4L_4]$, cyclic voltammetry was conducted on an aqueous solution of the cage. The voltammogram displayed a single quasi-reversible redox process at $E_{1/2}$ = 174 mV versus normal hydrogen electrode (NHE) (Figure S19), which is attributed to the Fe(II)/Fe(III) redox couple. The observation of only one set of redox peaks suggests the absence of effective electronic communication among the Fe(III) centers, corroborating the findings from EPR spectroscopy and solid-state magnetic measurements. This isolation between the Fe(III) centers likely contributes to the stability of the redox state under physiological conditions. To further assess the redox stability, we utilized the ascorbic acid test [39], a method involving the addition of excess ascorbic acid to the complex solution while continuously monitoring the characteristic absorption changes of ascorbic acid at 265 nm and the absorption of the complex via UV-vis spectroscopy. Our experiments demonstrated that the absorption of $K_{12}[Fe_4L_4]$ remained relatively stable, showing negligible changes over an extended period of 24 h in the presence of 10 equiv. of ascorbic acid (Figure S20). This indicates that $K_{12}[Fe_4L_4]$ maintains its structural integrity in a reducing environment, a property vital for *in vivo* imaging applications. The robust redox stability of $K_{12}[Fe_4L_4]$ cannot be rationalized by the relatively positive $E_{1/2}$ of its Fe(II)/Fe(III) redox couple, which is indicative of the complex's susceptibility to reduction. The unique coordination environment provided by the tri-catecholate moieties, in conjunction with the structural constraints imposed by the tetrahedral cage, likely contributes to a high reorganization energy associated with the redox process, which in turn renders it kinetically slow.

2.4 Host-guest chemistry exhibited by $K_{12}[Ga_4L_4]$

A pivotal aspect of this study involves exploiting host-guest interactions to develop multifunctional MRI contrast agents. Given the paramagnetic nature of $K_{12}[Fe_4L_4]$, which complicates NMR analysis, binding studies in aqueous solutions were conducted using the diamagnetic analogue, $K_{12}[Ga_4L_4]$. This strategy facilitated detailed NMR investigations. Similar anionic M(III) catecholate tetrahedral cages have demonstrated a propensity to bind cationic guests such as alkylamines and organometallic compounds through robust cation-π interactions, while their capacity to encapsulate neutral guests is notably more limited [40]. Initial experiments with simple neutral molecules like cyclohexane and (*R*)-limonene yielded two distinct sets of NMR signals (Figures S21 and S22), indicating that these guests experienced significant shielding effects within the cage cavity, leading to an upfield shift in NMR resonances. This encapsulation was corroborated by ^{1}H DOSY NMR, where both guest and host were observed to diffuse at the same rate, highlighting the effective encapsulation within the cage (Figures S23 and S24). However, tetrahedrally shaped molecules such as adamantane did not exhibit encapsulation. Additionally, other neutral molecules such as naphthalene, azobenzene derivatives, tetrahydrofuran, and 2-formylpyridine showed no signs of cage entry. These findings suggest that guest permeability is determined by a combination of factors such as hydrophobicity, shape complementarity between the cavity and the guest, and favorable cage-guest interactions. Inspired by Fujita's pioneering work on the encapsulation of fluorinated guests by metallocages, we hypothesized that similar methodologies might enhance the potential for dual-modality (^{1}H/^{19}F) MRI applications. Consequently, a variety of fluorine-substituted aromatic and aliphatic molecules, both hydrophilic and lipophilic, were tested. Despite these efforts, these molecules failed to effectively access the hydrophobic cavity of $K_{12}[Ga_4L_4]$, likely due to insufficient host-guest interactions (Figure S25). This limitation could be attributed to the smaller cavity size within our cages, which may not favor the aggregation of multiple fluorine molecules through fluorophilic interactions, a key driving force in successful encapsulation scenarios [41,42].

The encapsulation of the 2,2,6,6-tetramethylpiperidinyl-1-oxide (TEMPO) radical presents a particularly compelling aspect of our study. The paramagnetic nature of TEMPO typically leads to the broadening of NMR signals, complicating the direct confirmation of encapsulation using ^{1}H NMR alone (Figure S26). However, host-guest interactions between organic radicals and the cage can often be inferred from alterations in EPR spectroscopy signals. As illustrated in Figure 4a, adding $K_{12}[Ga_4L_4]$ to an aqueous solution containing TEMPO resulted in a progressive decrease in EPR signal intensity. This reduction in intensity, attributed to line broadening, indicates a slower tumbling motion of the encapsulated guest within the cage [43]. Furthermore, the introduction of a stronger binding guest, such as NEt_4^+, led to the complete recovery of the EPR signal intensity, suggesting competitive binding that displaces the encapsulated TEMPO. The binding affinity of TEMPO to $K_{12}[Ga_4L_4]$ was quantitatively assessed using isothermal titration calorimetry (ITC), yielding a binding constant of 3.30×10^4 M^{-1} (Figure 4b, c). Nitrogen oxide radicals, including TEMPO, have been explored as potential MRI contrast agents due to their unique electronic properties [44–47]. However, these radicals are typically rapidly reduced to diamagnetic hydroxylamines *in vivo*, with a half-life of only a few minutes [48,49]. This reduction behavior can be significantly influenced by the local chemical environment, which the cage structure is poised to modulate [50]. Therefore, our future research will concentrate on investigating how encapsulation

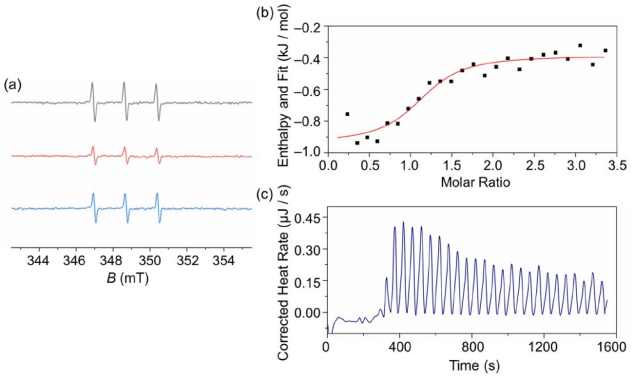

Figure 4 (Color online) (a) EPR spectra of TEMPO (top), TEMPO and $K_{12}[Ga_4L_4]$ (middle), and adding NEt_4Cl to a TEMPO and $K_{12}[Ga_4L_4]$ mixture (bottom) in water; TEMPO concentration: 2×10^{-5} M, $K_{12}[Ga_4L_4]$ concentration: 5×10^{-4} M, and NEt_4Cl concentration: 8×10^{-3} M; the ITC experiment involved titrating a 5.0 mM $K_{12}[Ga_4L_4]$ solution into a 0.5 mM TEMPO solution. (b) Raw data for sequential 25 injections (2 μL per injection) and (c) the apparent reaction heat is derived from integrating calorimetric traces.

within $K_{12}[Ga_4L_4]$ impacts both the stability and MRI contrast efficacy of TEMPO.

2.5 *In vitro* relaxometric studies

The relaxivity (r_1) of $K_{12}[Fe_4L_4]$ was evaluated under magnetic fields of 0.5 and 9.4 T, at temperatures of 32 and 22 °C respectively. The cage exhibited excellent proton relaxivity values of 5.41 mM^{-1} s^{-1} at 0.5 T, 32 °C and 5.51 mM^{-1} s^{-1} at 9.4 T, 22 °C. When normalized per iron atom, $K_{12}[Fe_4L_4]$ demonstrated a relaxivity of 1.28 mM^{-1} s^{-1} at 0.5 T, 32 °C, reflecting a 45% and 18% enhancement compared to mononuclear FeL^1_3 (0.88 mM^{-1} s^{-1}) and dinuclear $Fe_2L^2_3$ (1.07 mM^{-1} s^{-1}) complexes with catecholate ligands, respectively, as detailed in Table S1 (Supporting Information online) [24]. For comparison, $Fe_4L^3_6$, another cage used as a T_1-weighted contrast agent, reported r_1 values of 5.72 mM^{-1} s^{-1} at 1 T, 8.3 mM^{-1} s^{-1} at 1.4 T and 33 °C, and 8.7 mM^{-1} s^{-1} at 4.7 T and 37 °C, which are higher than those of $K_{12}[Fe_4L_4]$ under similar conditions likely due to differences in field strength and temperature conditions. Moreover, when compared to mononuclear iron(III) complexes with chelating ligands, such as EDTA (1.17 mM^{-1} s^{-1}), *t*CDTA (2.27 mM^{-1} s^{-1}), and *t*BPCDTA (1.56 mM^{-1} s^{-1}), the normalized relaxivity of $K_{12}[Fe_4L_4]$ remains comparable [51]. Recent studies suggest that optimizing parameters like electron spin relaxation (τ_e), rotational correlation time (τ_R), and second coordination sphere state could theoretically enhance the relaxivity (r_1) of Fe(III) complexes in magnetic fields exceeding 3.0 T. [39] However, at a high field strength of 9.4 T, $K_{12}[Fe_4L_4]$ does not demonstrate this anticipated increase in relaxivity. Instead, the relaxivity normalized to each iron atom declines to 1.38 mM^{-1} s^{-1}.

When evaluating $K_{12}[Fe_4L_4]$ as a potential Gd(III)-free alternative, it is essential to compare its performance with established GBCAs. For instance, Magnevist (Gd-DTPA), a clinical contrast agent, exhibits an r_1 of 4.27 mM^{-1} s^{-1}, which is higher per iron atom compared to $K_{12}[Fe_4L_4]$ [52]. However, considering the entire $K_{12}[Fe_4L_4]$ molecule, which contains four iron atoms, the r_1 value reaches 5.51 mM^{-1} s^{-1} at a lower field, surpassing that of Magnevist. Despite these comparisons, GBCAs retain advantages, particularly at higher relaxivities. Gianolio's group reported that Gd-L^4 displays an r_1 of 7.1 mM^{-1} s^{-1} at 0.5 T, which further increases to 26.5 mM^{-1} s^{-1} upon HAS [53]. Moreover, the unique structure of $K_{12}[Fe_4L_4]$, with its four Fe(III) centers coordinated by three catecholate ligands, results in a closed coordination sphere that lacks bound water molecules (q = 0). This structural arrangement indicates that the relaxivity of $K_{12}[Fe_4L_4]$ is primarily derived from outer-sphere water interactions, contrasting with the inner-sphere contributions typically observed in GBCAs.

A key advantage of $K_{12}[Fe_4L_4]$ lies in its favorable relaxivity (r_1) properties, which are further amplified by a reduction in the tumbling rate following protein binding. This enhancement is possibly facilitated through cation-π interaction, recognized as one of the strongest non-covalent interactions [40]. Recently, Gianolio *et al*. [53] explored the application of this particular mechanism of action in the domain of magnetic resonance contrast agents, utilizing a macrocyclic Gd-HPDO3A derivative functionalized with trisulfonated pyrene. Despite the trisulfonated pyrene imparting three negative charges to the agent, the mechanism of action remains the cation-π interaction between the amino residues in HSA and the pyrene ring. The crystal structure analysis of $K_{12}[Fe_4L_4]$ reveals that the four six-membered rings of the face-capped ligand of the cage are nearly planar, creating a substantial conjugation plane conducive to cation-π interactions. Dynamic light scattering (DLS) measurements indicated that the hydrodynamic of HSA in PBS buffer at pH of 7.4 was (7.5 ± 1.0) nm, aligning with previously reported literature values [54]. Upon mixing with $K_{12}[Fe_4L_4]$, the hydrodynamic diameter of mixture increased to (10.1 ± 1.6) nm, with the peak maximum of the size distribution shifting towards larger hydrodynamic diameters (Figure S27). This shift suggests a significant interaction between the HSA molecules and $K_{12}[Fe_4L_4]$ [55]. Additionally, the combination of HSA and $K_{12}[Fe_4L_4]$ also alters the electrokinetic (zeta) potential of the solution. The electrokinetic (zeta) potential of HSA is (−9.6 ± 1.4) mV, while that of HSA upon mixing $K_{12}[Fe_4L_4]$ results in an electrokinetic (zeta) potential of (–21.0 ± 0.1) mV. This more negative electrokinetic (zeta) potential, compared to that of HSA, implies agglutination with lower affinity [56]. The observed changes in hydrodynamic diameters and electrokinetic potential upon mixing HSA and $K_{12}[Fe_4L_4]$ provide positive evidence sup-

porting this possible interaction mechanism. This binding mechanism not only stabilizes the protein-cage complex but also significantly enhances the relaxivity, thereby improving the efficacy of the contrast agent. In the presence of HSA, relaxivities increased to 9.24 and 7.57 mM^{-1} s^{-1} at 0.5 and 9.4 T, respectively (Figures S28 and S29). To further study the impact of this interaction, the proton relaxation enhancement method was employed [57,58]. Initially, a solution of 0.12 mM $K_{12}[Fe_4L_4]$ was titrated with progressively increasing concentrations of HSA (Figure 5a). With rising HSA levels, the proton relaxation rate initially increased rapidly, indicative of effective binding interactions. This rate of relaxation plateaued upon saturation of the available protein binding sites. Beyond this saturation point, any further slight increase in the relaxation rate was attributed to the heightened solution viscosity resulting from increased HSA concentrations. Quantitative analysis of the titration data, as detailed in the Supporting Information online, determined that the inflection point for HSA binding occurred at concentrations between 0.03 and 0.04 mM. The calculated binding constant for $K_{12}[Fe_4L_4]$ with HSA was (6.1 ± 1.4) × 10^4 M^{-1}, demonstrating a strong interaction, with a relaxivity of HSA-bound complex (r_1^b) of 10.1 mM^{-1} s^{-1}. To further delineate the binding dynamics between $K_{12}[Fe_4L_4]$ and HSA, a series of experiments with stepwise increases in $K_{12}[Fe_4L_4]$ concentration were conducted, while maintaining a constant HSA concentration of 0.04 mM (Figure 5b). The proton relaxation rate increased proportionally with the concentration of $K_{12}[Fe_4L_4]$ until reaching an inflection point at 0.12 mM. Below this concentration, HSA bind almost quantitatively to $K_{12}[Fe_4L_4]$. Upon reaching the 0.12 mM concentration, the binding sites on HSA became saturated, leading to a slight decrease in relaxivity. From these results, the binding ratio of $K_{12}[Fe_4L_4]$ to HSA is inferred to be 3:1 under the experimental conditions studied. This strong affinity and specific binding stoichiometry highlight the potential of $K_{12}[Fe_4L_4]$ as an effective blood-pool MRI contrast agent, facilitated by its robust interaction with serum proteins.

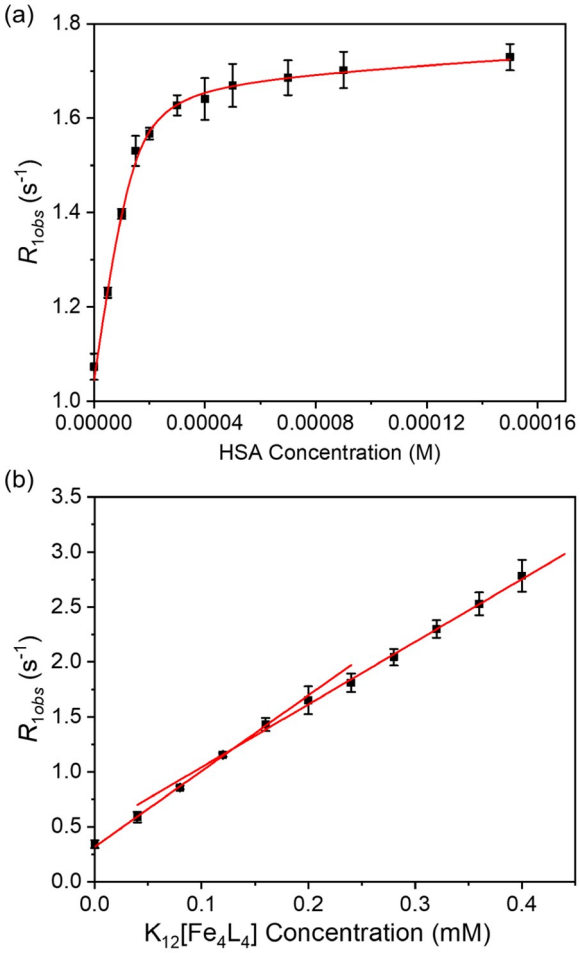

Figure 5 (Color online) The binding parameters of $K_{12}[Fe_4L_4]$ with HSA were measured using proton relaxation enhancement, which involved (a) titration of 0.12 mM $K_{12}[Fe_4L_4]$ with increasing concentrations of HSA, and (b) titration of 0.04 mM HSA with increasing concentrations of $K_{12}[Fe_4L_4]$.

2.6 *In vivo* MRI studies

All procedures involving animals were approved by the Animal Welfare and Research Ethics Committee at the Innovation Academy for Precision Measurement Science and Technology, Chinese Academy of Sciences (APM23024T). The cytotoxicity of $K_{12}[Fe_4L_4]$ was initially evaluated using MTT assays on Mlg2908 mouse lung fibroblasts. Results indicated that cell viability remained above 90% across a range of concentrations (0–200 μM) after 12 h of incubation, with no significant cytotoxic effects observed at the administered doses (Figure S30). Before *in vivo* MRI analysis, the *in vivo* biocompatibility of $K_{12}[Fe_4L_4]$ was also conducted. $K_{12}[Fe_4L_4]$ (dose: 0.01 mM kg^{-1}) or physiological saline (control) was intravenously injected into the healthy Balb/c mice, and then blood analysis and haematoxylin and eosin (H&E) staining of major organs were performed post-24 h. The results illustrated no obvious inflammation or lesions in the heart, liver, spleen, lung, and kidney, and the blood biochemical indices of liver and kidney function in $K_{12}[Fe_4L_4]$ and control groups were within normal limits (Figures S31 and S32), thereby validating its safety for *in vivo* application. Subsequent investigations assessed the MRI performance of $K_{12}[Fe_4L_4]$ in healthy Balb/c mice using a 9.4 T MRI scanner. For a reliable comparison, *in vivo* results for $K_{12}[Fe_4L_4]$ were benchmarked against those for Gd (HP-DO3A) (ProHance), administered at an identical dose of 0.01 mmol kg^{-1}. Post-intravenous injection of $K_{12}[Fe_4L_4]$, significant contrast enhancements were observed in the liver, kidneys, and spleen. Specifically, the maximal percentage signal enhancements were 47.7%, 42.7%, and 39.3% respectively, for these organs in the $K_{12}[Fe_4L_4]$ group, com-

pared to 8.3%, 6.2%, and 2.3% in the ProHance group (Figure 6). This indicates that the enhancements in the $K_{12}[Fe_4L_4]$ group were approximately 5.7, 6.9, and 17.1 times those observed with ProHance, suggesting markedly superior imaging efficacy of $K_{12}[Fe_4L_4]$ at low doses. Moreover, while ProHance-mediated MRI contrast enhancements in the liver, kidneys, and spleen decreased significantly within 40 min, the $K_{12}[Fe_4L_4]$ group maintained robust MRI contrast in these tissues for up to 8 h post-injection (Figure 6c). This prolonged retention time is attributed to the blood-pool agent characteristics of $K_{12}[Fe_4L_4]$, stemming from its strong binding affinity for serum albumin, which facilitates long-term monitoring of targeted tissues. *In vivo* imaging monitoring in mice revealed that $K_{12}[Fe_4L_4]$ is primarily metabolized by the liver and kidneys, similar to $Fe_4L^3{}_6$, which is cleared through a hepatobiliary mechanism [2].

3 Conclusions

In this study, we successfully synthesized and characterized two face-capped M_4L_4 MOCs. The $K_{12}[Fe_4L_4]$ cage, in particular, emerged as an effective T_1-weighted MRI contrast agent, exhibiting exceptional longitudinal relaxivity (r_1). With a relaxivity of 5.41 mM^{-1} s^{-1} at 32 °C and 0.5 T that increases to 9.24 mM^{-1} s^{-1} in the presence of HSA, $K_{12}[Fe_4L_4]$ offers a promising Gd(III)-free alternative. This cage combines notable water solubility, stability, and a robust protein-binding capability, contributing to its superior imaging qualities. *In vivo* MRI studies at a low dosage of 0.010 mmol kg^{-1} revealed that $K_{12}[Fe_4L_4]$ provides enhanced imaging and extended retention time compared to the commercially available contrast agent ProHance. Furthermore, we extended our investigation to the $K_{12}[Ga_4L_4]$ cage, its diamagnetic counterpart, examining its host-guest chemistry, particularly with neutral guests. Notably, $K_{12}[Ga_4L_4]$ demonstrated an ability to encapsulate the TEMPO organic radical, a finding of interest due to the radical's inherent imaging capabilities. The cage's structure effectively restricts these radicals within its cavity, which can enhance their stability in reducing environments and increase their rotational correlation time, thereby potentially improving image contrast. Our future research will delve further into this phenomenon, aiming to develop multi-modality MRI contrast agents that harness both the magnetic and structural properties of these unique cages. Metal-organic cages as MRI contrast agents present both significant challenges and promising opportunities. Several key limitations must be addressed: primarily, achieving optimal water solubility while maintaining cage stability remains a critical challenge. Additionally, the careful design and screening of ligands for cage construction requires extensive research and development. From a commercial perspective, the cost-effectiveness of these materials poses a potential barrier to widespread implementation. Nevertheless, these challenges are counterbalanced by compelling opportunities. The unique host-guest chemistry of metal-organic cages offers considerable potential for advancement in magnetic resonance contrast agent development. Furthermore, the versatility in ligand modification and the capability for cage-cage responsive transitions present promising avenues for future innovations in this field. When addressing challenges, this work not only

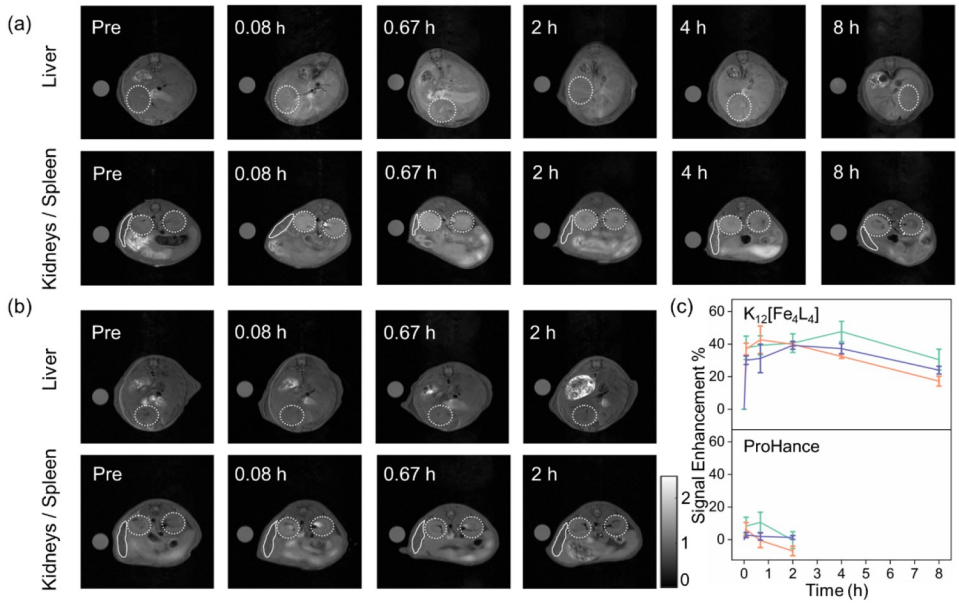

Figure 6 (Color online) *In vivo* ^1H T_1-weighted MRI of healthy Balb/c mice pre- and post-*i.v.* injected with (a) $K_{12}[Fe_4L_4]$ or (b) ProHance (0.01 mmol kg^{-1}) in physiological saline displayed in the axial section and (c) the corresponding percentage signal enhancement of the liver, kidneys, and spleen as a function of time (standard error of the mean, n = 3).

underscores the significance of careful structural design in developing MOC-based contrast agents but also represents a step moving beyond traditional gadolinium-based agents.

Acknowledgements This work was supported by the National Natural Science Foundation of China (22471016, 22371015). We extend our gratitude to Professor Lei Zhang and Ms. Zhao-Qing Liu of the Wuhan Institute of Physics and Mathematics for their invaluable assistance with the measurements and interpretation of cytotoxicity and *in vivo* MRI studies. Additionally, we appreciate the support of Professor Hao-Ling Sun and Ms. Xin Wang from the College of Chemistry at Beijing Normal University for their help with the T1 experiments of $K_{12}[Fe_4L_4]$ at 0.5 T. The single-crystal X-ray diffraction (SC-XRD) data were collected at the BL17B beamline of the National Center for Protein Sciences at the Shanghai Synchrotron Radiation Facility. Furthermore, we acknowledge the technical support provided by the Chemistry and Chemical Experiment Center and the Analysis & Testing Center of the Beijing Institute of Technology.

Conflict of interest The authors declare no conflict of interest.

Supporting information The supporting information is available online at http://chem.scichina.com and http://link.springer.com/journal/11426. The supporting materials are published as submitted, without typesetting or editing. The responsibility for scientific accuracy and content remains entirely with the authors.

1 Wahsner J, Gale EM, Rodríguez-Rodríguez A, Caravan P. *Chem Rev*, 2018, 119: 957–1057
2 Pierre VC, Allen MJ, Caravan P. *J Biol Inorg Chem*, 2014, 19: 127–131
3 Aime S, Botta M, Fasano M, Terreno E. *Chem Soc Rev*, 1998, 27: 19–29
4 Runge VM. *Invest Radiol*, 2017, 52: 317–323
5 Kras EA, Snyder EM, Sokolow GE, Morrow JR. *Acc Chem Res*, 2022, 55: 1435–1444
6 Yu M, Ward MB, Franke A, Ambrose SL, Whaley ZL, Bradford TM, Gorden JD, Beyers RJ, Cattley RC, Ivanović-Burmazović I, Schwartz DD, Goldsmith CR. *Inorg Chem*, 2017, 56: 2812–2826
7 Grobner T. *Nephrol Dial Transplant*, 2006, 21: 1104–1108
8 Marckmann P, Skov L, Rossen K, Dupont A, Damholt MB, Heaf JG, Thomsen HS. *J Am Soc Nephrol*, 2006, 17: 2359–2362
9 Kanda T, Fukusato T, Matsuda M, Toyoda K, Oba H, Kotoku J', Haruyama T, Kitajima K, Furui S. *Radiology*, 2015, 276: 228–232
10 Kuźnik N, Wyskocka M. *Eur J Inorg Chem*, 2016, 2016: 445–458
11 Snyder EM, Asik D, Abozeid SM, Burgio A, Bateman G, Turowski SG, Spernyak JA, Morrow JR. *Angew Chem Int Ed*, 2019, 59: 2414–2419
12 Bertini I, Luchinat C, Parigi G, Ravera E. Transition metal ions: shift and relaxation. In: Morrissey K, Ed. *NMR of Paramagnetic Molecules: Applications to Metallobiomolecules and Models. Chapter 7*. Amsterdam: Elsevier, 2016. 175–253
13 Asik D, Abozeid SM, Turowski SG, Spernyak JA, Morrow JR. *Inorg Chem*, 2021, 60: 8651–8664
14 Wyskocka-Gajda M, Przypis Ł, Olesiejuk M, Krawczyk T, Kuźnik A, Nawara K, Minoshima M, Sugihara F, Kikuchi K, Kuźnik N. *Eur J Med Chem*, 2021, 211: 113086
15 Caulder DL, Raymond KN. *Acc Chem Res*, 1999, 32: 975–982
16 Cook TR, Stang PJ. *Chem Rev*, 2015, 115: 7001–7045
17 Chen LJ, Yang HB, Shionoya M. *Chem Soc Rev*, 2017, 46: 2555–2576
18 Zhang YY, Gao WX, Lin L, Jin GX. *Coord Chem Rev*, 2017, 344: 323–344
19 Pullen S, Clever GH. *Acc Chem Res*, 2018, 51: 3052–3064
20 Sun Y, Chen C, Liu J, Stang PJ. *Chem Soc Rev*, 2020, 49: 3889–3919
21 Pan M, Wu K, Zhang JH, Su CY. *Coord Chem Rev*, 2019, 378: 333–349
22 Ward MD, Hunter CA, Williams NH. *Acc Chem Res*, 2018, 51: 2073–2082
23 Rizzuto FJ, von Krbek LKS, Nitschke JR. *Nat Rev Chem*, 2019, 3: 204–222
24 Wang R, An L, He J, Li M, Jiao J, Yang S. *J Mater Chem B*, 2021, 9: 1787–1791
25 Sokolow GE, Crawley MR, Morphet DR, Asik D, Spernyak JA, McGray AJR, Cook TR, Morrow JR. *Inorg Chem*, 2022, 61: 2603–2611
26 Caulder DL, Powers RE, Parac TN, Raymond KN. *Angew Chem Int Ed*, 1998, 37: 1840–1843
27 Caulder DL, Brückner C, Powers RE, König S, Parac TN, Leary JA, Raymond KN. *J Am Chem Soc*, 2001, 123: 8923–8938
28 Davis AV, Raymond KN. *J Am Chem Soc*, 2005, 127: 7912–7919
29 Du K, Zemerov SD, Hurtado Parra S, Kikkawa JM, Dmochowski IJ. *Inorg Chem*, 2020, 59: 13831–13844
30 Peng XX, Gao S, Zhang JL. *Eur J Inorg Chem*, 2022, 2022: e202100953
31 Einstein A. *Annalen der Physik*, 1905, 322: 549–560
32 Fujita M, Oguro D, Miyazawa M, Oka H, Yamaguchi K, Ogura K. *Nature*, 1995, 378: 469–471
33 Yeh RM, Xu J, Seeber G, Raymond KN. *Inorg Chem*, 2005, 44: 6228–6239
34 Liu ZK, Yao ZS, Tao J. *Inorg Chem*, 2021, 60: 10291–10301
35 Weisser JT, Nilges MJ, Sever MJ, Wilker JJ. *Inorg Chem*, 2006, 45: 7736–7747
36 Percástegui EG, Mosquera J, Nitschke JR. *Angew Chem Int Ed*, 2017, 56: 9136–9140
37 Turyan YI, Kohen R. *J Electroanal Chem*, 1995, 380: 273–277
38 Koppenol WH, Hider RH. *Free Radical Biol Med*, 2019, 133: 3–10
39 Baranyai Z, Carniato F, Nucera A, Horváth D, Tei L, Platas-Iglesias C, Botta M. *Chem Sci*, 2021, 12: 11138–11145
40 Ma JC, Dougherty DA. *Chem Rev*, 1997, 97: 1303–1324
41 Krafft M. *Adv Drug Deliver Rev*, 2001, 47: 209–228
42 Hoang KC, Mecozzi S. *Langmuir*, 2004, 20: 7347–7350
43 Nicholas JD, Chechik V. *J Phys Chem B*, 2020, 124: 5646–5653
44 Vallet P, van Haverbeke Y, Bonnet PA, Subra G, Chapat JP, Muller RN. *Magn Reson Med*, 1994, 32: 11–15
45 Winalski CS, Shortkroff S, Mulkern RV, Schneider E, Rosen GM. *Magn Reson Med*, 2002, 48: 965–972
46 Emoto MC, Yamada K, Yamato M, Fujii HG. *Neurosci Lett*, 2013, 546: 11–15
47 Bye N, Hutt OE, Hinton TM, Acharya DP, Waddington LJ, Moffat BA, Wright DK, Wang HX, Mulet X, Muir BW. *Langmuir*, 2014, 30: 8898–8906
48 Hyodo F, Matsumoto K, Matsumoto A, Mitchell JB, Krishna MC. *Cancer Res*, 2006, 66: 9921–9928
49 Zhelev Z, Bakalova R, Aoki I, Lazarova D, Saga T. *ACS Chem Neurosci*, 2013, 4: 1439–1445
50 Rajca A, Wang Y, Boska M, Paletta JT, Olankitwanit A, Swanson MA, Mitchell DG, Eaton SS, Eaton GR, Rajca S. *J Am Chem Soc*, 2012, 134: 15724–15727
51 He L, Wang H, Zeng Z, Zhong L, Tang Q, Yu J, Tian J, Liu T, Zhu J. *J Med Chem*, 2024, 67: 8630–8641
52 Rohrer M, Bauer H, Mintorovitch J, Requardt M, Weinmann HJ. *Investig Radiol*, 2005, 40: 715–724
53 Stefania R, Palagi L, Di Gregorio E, Ferrauto G, Dinatale V, Aime S, Gianolio E. *J Am Chem Soc*, 2024, 146: 134–144
54 Leggio C, Galantini L, Pavel NV. *Phys Chem Chem Phys*, 2008, 10: 6741–6750
55 Haeri HH, Eisermann J, Schimm H, Büscher A, Hoyer P, Hinderberger D. *J Med Chem*, 2023, 66: 12115–12129
56 Kajani AA, Pouresmaeili A, Kamali M. *RSC Adv*, 2024, 14: 16801–16808
57 Aime S, Chiaussa M, Digilio G, Gianolio E, Terreno E. *J Biol Inorg Chem*, 1999, 4: 766–774
58 Palagi L, Di Gregorio E, Costanzo D, Stefania R, Cavallotti C, Capozza M, Aime S, Gianolio E. *J Am Chem Soc*, 2021, 143: 14178–14188